STScI | SPACE TELESCOPE SCIENCE INSTITUTE

WFC3 Instrument Science Report 2022-07

WFC3/IR Photometric Stability Stellar Cluster Study

V. Bajaj, A. Calamida, J. Mack, D. Som

October 13, 2022

Abstract

The infrared channel of Wide Field Camera 3 (WFC3) on the Hubble Space Telescope (HST) is frequently used to obtain precision photometric measurements. We investigate the change in the sensitivity of the IR channel over time by comparing photometry of outer, less crowded regions of stellar cluster images at multiple epochs. The channel appears to be losing sensitivity at a rate of approximately 0.13±.02% per year with no apparent wavelength dependence, though the slope and observation dates vary from cluster to cluster. Staring mode observations of the standard stars appear to show more inconsistent results, even within the same filter, but this is likely due to the presence of systematics such as detector preconditioning from prior observations.

1. Introduction

For over a decade the infrared (IR) channel of the Wide Field Camera 3 (WFC3) aboard the Hubble Space Telescope (HST) has been the preeminent near-infrared instrument available to image a variety of targets that would be difficult, if not impossible to image from the ground. As a result, the archive of HST data spans a wide variety of objects and a long baseline of measurement, serving as a foundation for many JWST science programs. To maximize the scientific value of the data, the evolution of the performance of the instrument must be characterized.

Other HST instruments, including the UVIS channel of WFC3 show clear evidence of a change in sensitivity over the instrument's lifetime (Calamida et al. (2021)). While these are

typically measured via regular monitoring of spectrophotometric standard stars (typically brighter white dwarf stars), the IR photometric measurements of these standard stars are not able to confirm the existence of sensitivity changes, due to insufficient photometric repeatability (Bajaj, Calamida, and Mack (2021)) yielding poor measurement significance. However, the IR channel has been used many times over the years to image a number of stellar clusters, for both calibration and science programs. If a cluster has been imaged multiple times in a given filter with a large enough baseline in between observations, and using the same observational strategy, then changes in sensitivity can be measured by comparing photometry of many individual stars over multiple epochs. In principle, this should reduce contributions of Poisson error to the overall uncertainty substantially, as an individual image may contain hundreds or thousands of measurable stars (as compared to a measurement per image in the case of the standard stars).

In practice, however, the change in IR photometric response due to observational configuration often presents confounding factors to photometric analysis (Bajaj, Calamida, and Mack (2021)). Thus it is crucial that the repeated images not only use the same filter, and point to the same region, but use the same observational parameters such as exposure time (sample sequence/number of samples), image sequencing, and dither patterns as the previous epoch. Repeating the observations as closely as possible should remove the dependence on observation strategy, and allow the relative measurement of fluxes of the stars over time to determine the sensitivity change. Matching the orientation of previous observations further minimizes spatial effects (i.e. flat field errors) and keeps contamination from diffraction spikes consistent, though it is not always possible to use the same orient angles.

With this further constraint applied, three suitable targets were found to have data already present in the HST archive, and were then followed up with additional observations in 2021/2022, consisting of data in the F110W and F160W filters.

Images taken in the outer regions (to lessen the effects of crowding compared to the cores) of the three clusters Messier 4 (M4), 47 Tucanae (47 Tuc), and Omega Centauri (ω Cen) were used in this study. Information regarding the programs in which these data were taken are listed in Appendix A. Data for each of the targets were downloaded recently from the MAST archive to ensure the calibrations used were all consistent and up to date.

2. Methods

Photometry and Matching

All of the calibrated `flt.fits` images of the targets, processed through `calwf3` were run through the `hst1pass` software[1] (Anderson (2022)) to obtain precise positions from PSF fitting for the stars in the images. Minimum separation parameters were set to find local maxima (peaks) isolated by at least 4 pixels, and flux limits were set to measure stars within the 4 magnitudes below saturation. The images were first aligned to Gaia DR2 (Gaia Collaboration et al. (2021)) using the methodology described in Bajaj (2017). A second, refining alignment pass, aligning the data for a given target to each other, was also performed, to minimize the relative astrometric error. Both alignments were completed using

[1] https://github.com/spacetelescope/wfc3_photometry

Target	RA, Dec	Filters	Epochs	Dates	Distance	R_{core}	Density
47 Tuc	5.627°, -72.068°	F160W	20	2009-2022	∼7'	0.36'	∼0.3
M4	245.921°, -26.504°	F110W, F160W	5, 3	2016-2022	∼2'	1.16'	∼0.25
ω Cen	201.392°, -47.466°	F110W, F160W	3, 3	2015-2022	∼12'	2.37'	∼0.5
ω Cen (core)	201.694°, -47.478°	F160W	44	2015-2022	0'	2.37'	>10

Table 1: Targets analyzed in this investigation. The Distance column refers to the approximate distance (in arcminutes) of the observed field from the center of the cluster, R_{core} is the core radius, and Density is an estimate of the number of stars per square arcsecond (the ω Cen core is extremely crowded, and stars are often not easily resolved). The ω Cen core data is presented to compare to prior work, but is not ideal for this analysis (see Section 4). See the appendix for more information on each target, including the individual exposure information.

the DrizzlePac function `TweakReg` (Fruchter et al. (2010)), with the catalogs from `hst1pass` as inputs. The astrometrically aligned catalogs were then matched into a master catalog, containing records of stars that were measured in multiple exposures for each of the unique pairs of target and filter via functionality in the The Astropy Collaboration et al. (2018) package.

In contrast to the work of Kozhurina-Platais and S. Baggett (2020), the PSF fit magnitudes from `hst1pass` were not used in the analysis to determine the sensitivity changes. Instead, using the positions from the `hst1pass` catalogs, aperture photometry was performed on the stars using `Photutils` (Bradley et al. (2017)) and implementation of the background measurement and error formulae described in Davis (1987). While aperture photometry does make the absolute measurement of the star's flux more vulnerable to crowding or blending, it removes systematic factors that can occur when fitting PSFs via `hst1pass` (i.e. variable PSF fits due to epoch-dependent source blending), and still allows the relative comparison of flux over time. The choice of fields not centered on the clusters for this study allows the crowding effects to be less impactful.

The aperture photometric parameters were set to the same values across all of the targets. Aperture radii of 3 pixels were used, as this radius balances the effects of PSF variability due to breathing in smaller apertures with the increased noise of larger apertures (Bajaj, Calamida, and Mack (2021)). To measure the background, a 3-sigma-clipped mean was calculated in an annulus around each source with inner and outer radii of 9 and 13 pixels, respectively.

Observation Count and Flux Range

Due to slight variations in observational configuration and observation dates (which changes the roll angle of the telescope), the actual portions of the sky imaged varied from epoch to epoch. Thus, the number of measurements for each star varied. To avoid systematically biasing the sensitivity change measurements, varying constraints were applied to the selection of stars used in the final measurements. Only stars within a certain brightness range (to reduce Poisson noise contribution and avoid saturation), and above a minimum threshold for number of detections across the sample of images for a given target (to have measurements over a longer baseline) were included in the final computations. The criteria slightly varied for each cluster, and are detailed in the results section.

First Images

As described in Bajaj (2019), the effects of persistence artificially move the measured flux of a star higher. The strength of the effect is more than sufficient to obscure any trends in the change of sensitivity; moreover observations of stellar clusters are often prone to self persistence, especially when large dithers are not used between exposures. To mitigate these effects, the computations of the sensitivity change were performed twice. The first computation included all the images for a given target/filter combination, which, if present, would suffer from the effects of self persistence. The second computation used only the first image from each visit, which would only be affected by external persistence (persistence from other observations), rather than persistence from exposures previously taken in the same visit, which is more severe. The second pass trades the number of individual measurements of a star for increased measurement quality by reducing potential systematic errors.

Sensitivity Change Computation

Two methods of relative measurement were used to examine how the sensitivity evolves over time. The first method first computed the median magnitude for each star across all the images in which the star was detected. The magnitude of a star, measured in each image, was then subtracted from the star's median magnitude, which we will call the magnitude offset. For each image the median magnitude offset of all stars in that image was recorded. The median magnitude offset was compared to the exposure date of each of the images (so each epoch may contribute multiple points), and a linear fit performed to obtain a measurement of the change in magnitude per year. Because the change in magnitude over the mission lifetime is assumed to be small, the change in magnitude is nearly equal to the fractional difference (percentage change/100), and can thus be used as a measurement of sensitivity change. The reported errors are simply the standard error of the fit slope.

The second, relative, method simply compared each star's magnitude measurements over time with the exposure date of the corresponding images. A linear fit was performed for each star, resulting in a measurement of change in magnitude per year for every star by extracting the slope of the fit. The median of these slopes was then computed to estimate the change in sensitivity.

3. Results

The resulting sensitivity change measurements described above are presented individually for each target below.

47 Tuc (F160W)

Observations of the relevant field of 47 Tuc were taken regularly in the F160W filter starting in 2010 and then ending in late 2013 as a part of the IR linearity monitor. A one-visit follow up set of observations were taken in 2022 to better constrain the sensitivity change rate. Stars that appeared in 95 of the 100 images or more, with STMag of 22.5 or less were selected for the analysis. A constraint of both magnitude standard deviations and mean PSF fit quality of 0.05 (total absolute residual divided by fit flux, see Anderson (2022)) or less was applied as a further limit. In this case, the -0.12±.02%/yr sensitivity change calculated from the median magnitude offset of all the images is consistent with -0.10±.04%/yr calculated from just the first images of each visit, to one sigma (see figure 1). Median slopes of -0.12±.01%/yr and -0.10±.01%/yr were calculated for all the images and the first images respectively (figures 2 and 3). It should be noted that the earlier visits of F160W contain more images (the larger number of yellow points early on in Figure 1) than the later visits, and large dithers were not employed for the additional images in those visits. This lack of dithering leads to more persistence, artificially driving the slope to be steeper when computed from all the images, compared to just the first images. Though the first four years of observation appear to show little to no change in sensitivity (especially when considering just the first images), the 2022 measurements reveal a small decrease in measured flux. When excluding the last epoch of data (2022), the slopes for all the images steepens to -0.17±0.05%/yr (likely due to strong persistence early on), whereas the slope for just the first images flattens to -0.04±0.11%/yr. This discrepancy may point to a non linear sensitivity loss, though the larger error on the slope from the first images does not strongly support this. To lessen the bias of the slope, additional measurements of 47 Tuc will be taken in coming cycles.

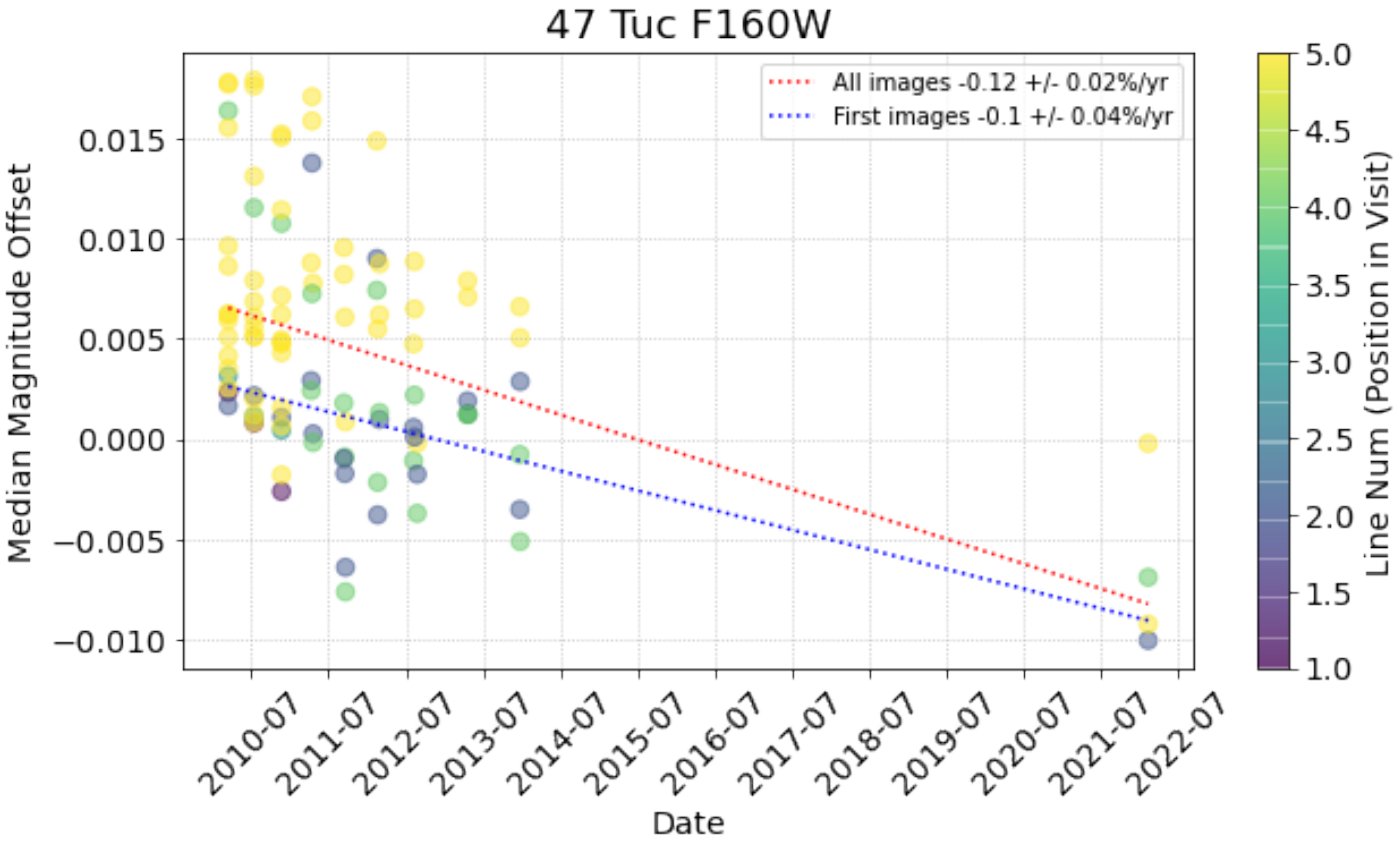

Figure 1: Median magnitude offset for the 47 Tuc F160W images. The color of the points corresponds to the chronological position (LINENUM) in each visit when an exposure was taken.

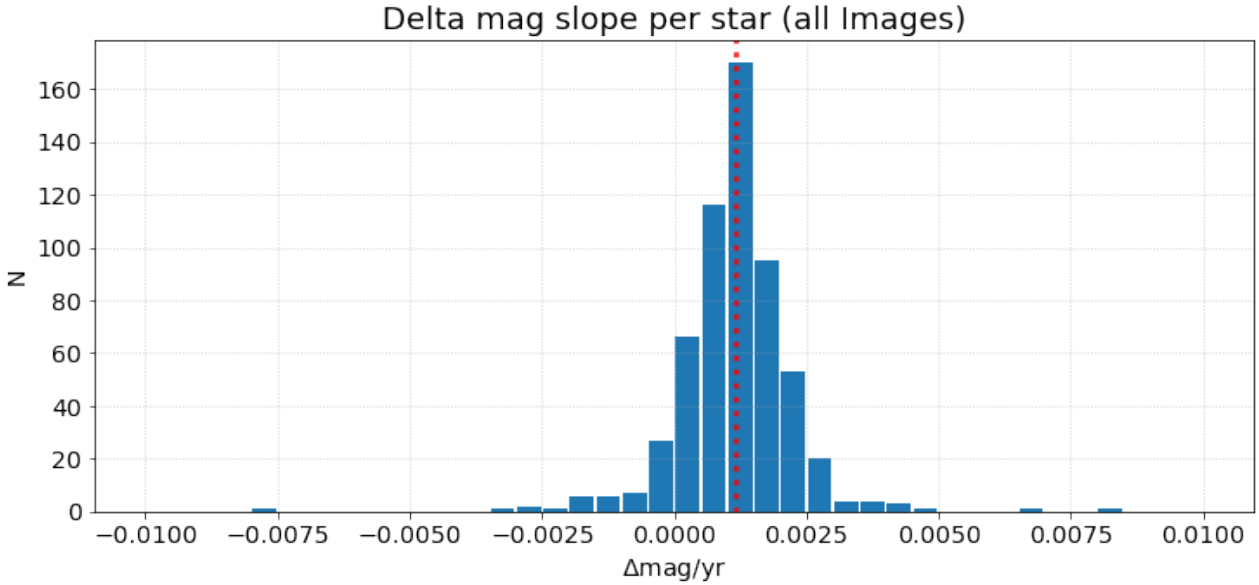

Figure 2: Slopes for the selected stars in the 47 Tuc F160W images, sampling from all of the images. The median position is denoted by the vertical red line. Note that a positive value of Δmag/yr reflects increasing magnitude (loss of measured flux).

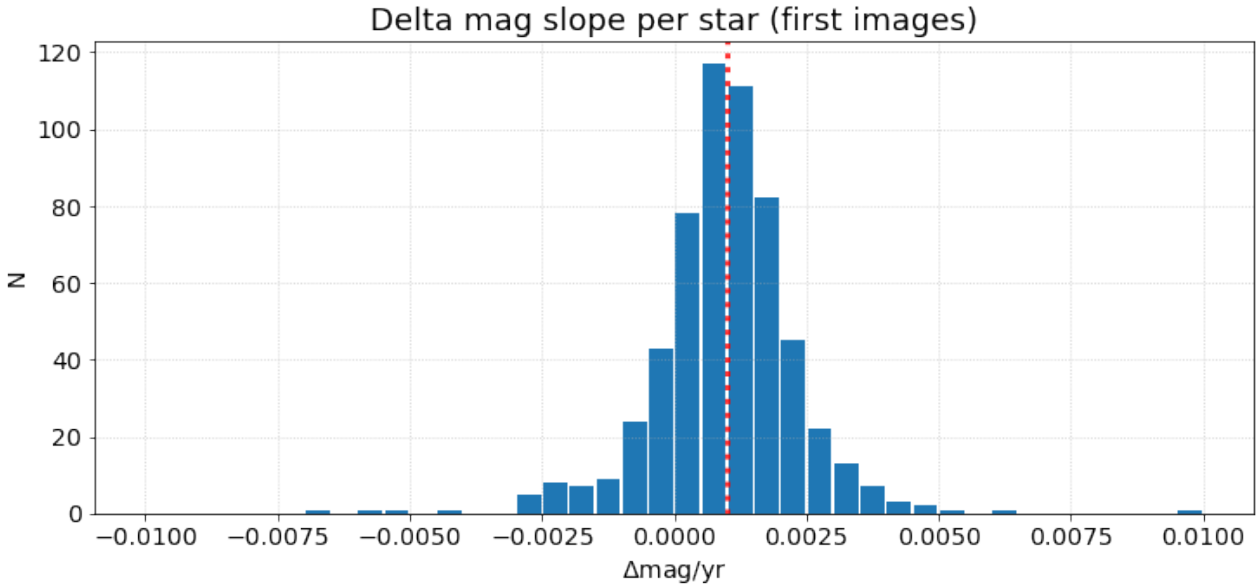

Figure 3: Slopes for the selected stars in the 47 Tuc F160W images only, sampling from the first images. The median position is denoted by the vertical red line. Note that a positive value of Δmag/yr reflects increasing magnitude (loss of measured flux).

M4

The images of the outer regions of M4 were taken in 2012, 2017, 2021, and 2022 in F110W, and 2012, 2021, and 2022 for F160W as a part of programs 12602, 14725, and 16512. With the exception of 2012, the F160W images were taken immediately after the F110W images in a given visit, thus there is only a single epoch for where F160W was taken as the first image of a visit. In 2012, a 4 point dither of about three pixels was used between exposures, however later visits used a larger dither of approximately 28 pixels between subsequent exposures, resulting in better persistence mitigation.

F110W

Stars detected in at least 15 images, with STMAGs brighter than 21 and mean fit quality values of 0.06 (slightly higher to allow more stars) and below were selected for the analysis. The F110W median magnitude offset yielded sensitivity changes of -0.2±.02%/yr and -0.14±.02%/yr for all the images and just the first images, respectively. Median slopes of -0.19±.01%/yr and -0.14±.01%/yr were calculated for the two sets of images.

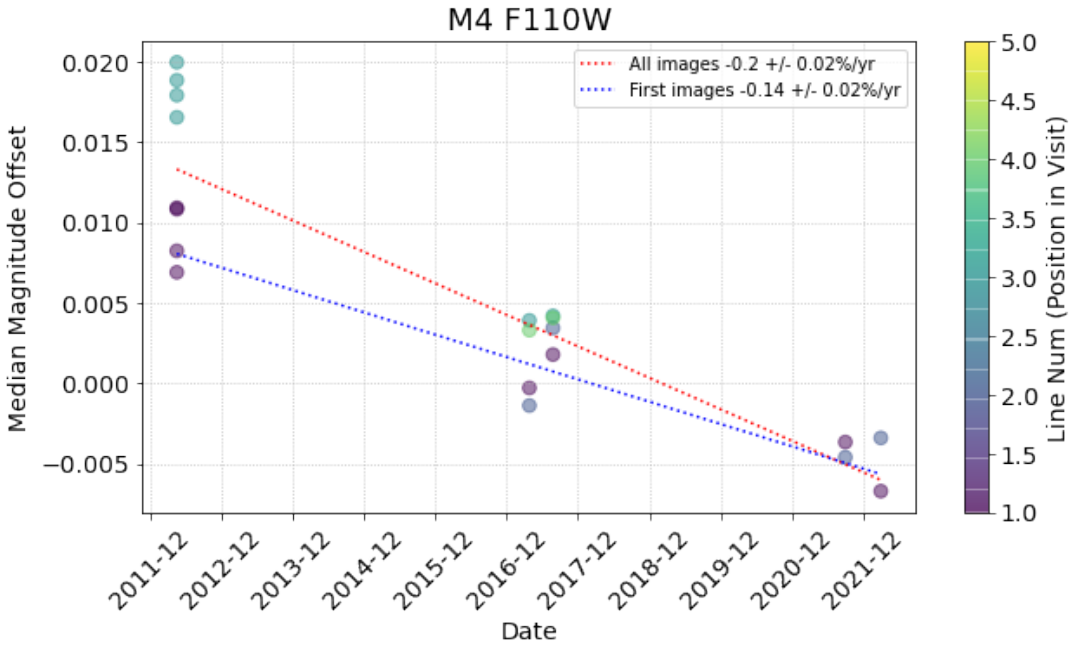

Figure 4: Median magnitude offset for the M4 F110W images. The color of the points corresponds to the chronological position (LINENUM) in each visit when an exposure was taken.

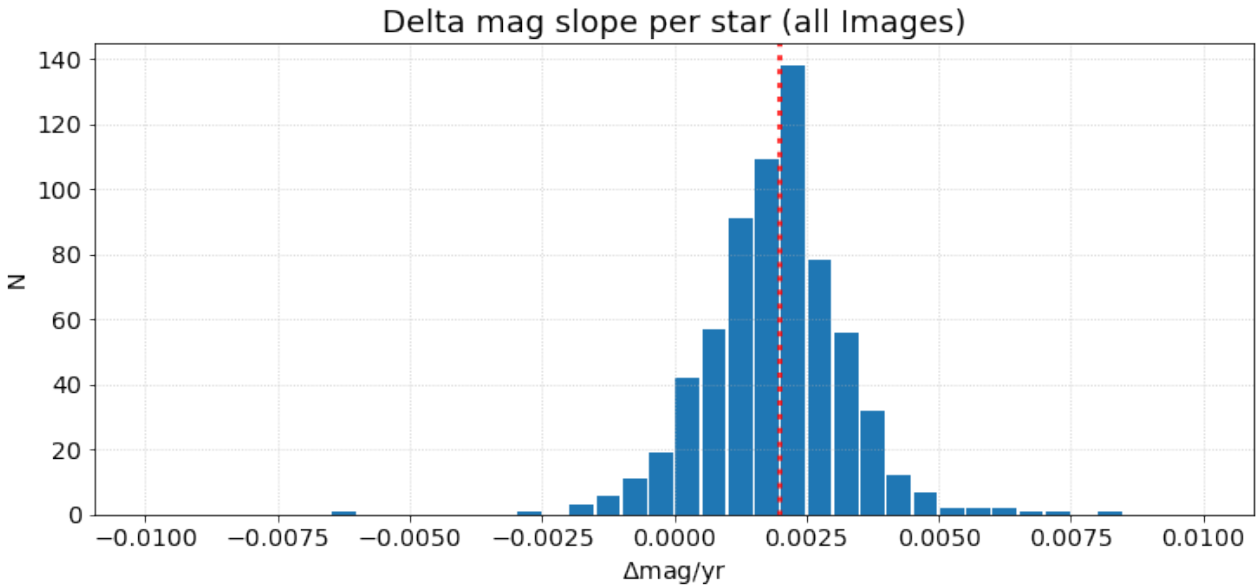

Figure 5: Slopes for the selected stars in the M4 F110W images, sampling from all of the images. The median position is denoted by the vertical red line. Note that a positive value of Δmag/yr reflects increasing magnitude (loss of measured flux).

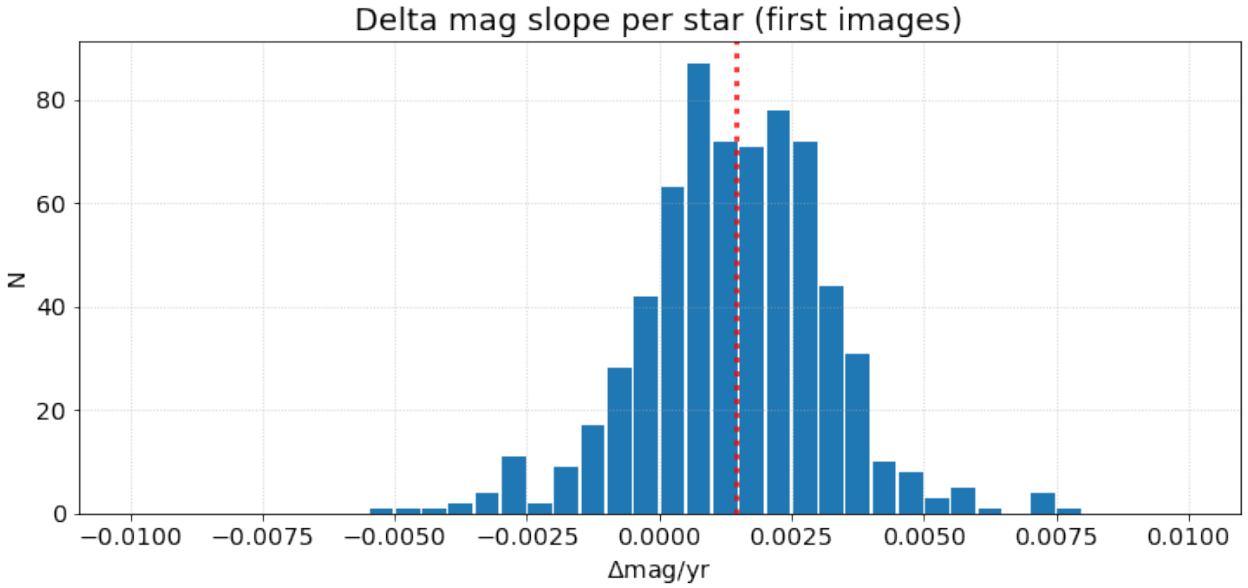

Figure 6: Slopes for the selected stars in the M4 F110W images, sampling from the first images. The median position is denoted by the vertical red line. Note that a positive value of Δmag/yr reflects increasing magnitude (loss of measured flux).

F160W

The same selection criteria for F110W selected for the analysis. The F160W median magnitude offset yielded sensitivity change of -0.14±.03%/yr for all the images. A median slope of -0.14±.01%/yr was calculated for all the images. Since there is only a singular first image (as the F160W images followed the F110W in all but one visit), there are no slope measurements for first images. It should be noted that many of the images from 2012 are affected by persistence, and though the later images may be as well, the 2012 images are likely much more affected, due to the use of the same dither positions (as opposed to consistently using unique positions), as discussed in Bajaj (2019). This biases the slope to be steeper than observations not affected persistence.

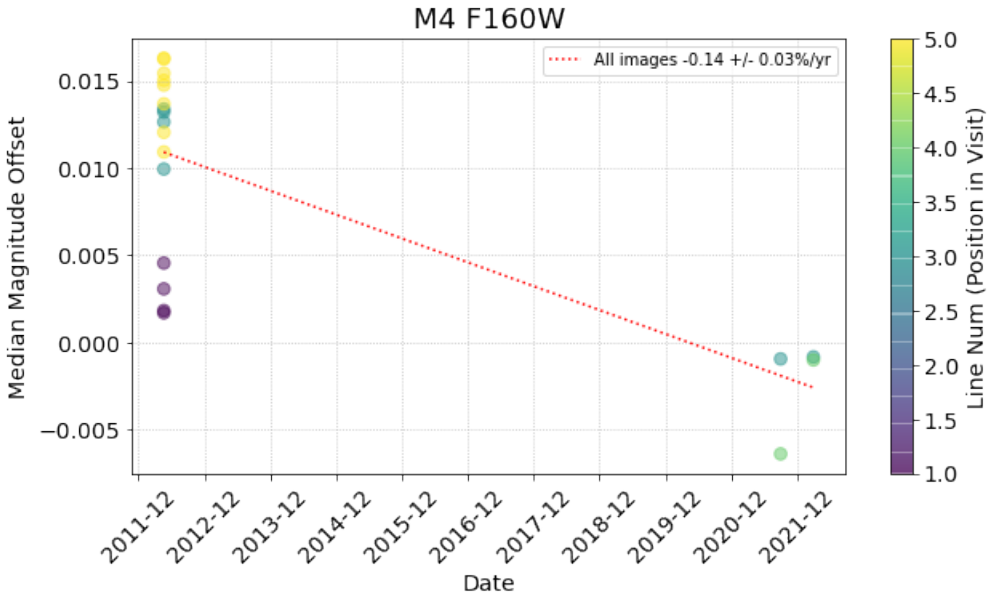

Figure 7: Median magnitude offset for the M4 F160W images. The color of the points corresponds to the chronological position (LINENUM) in each visit when an exposure was taken.

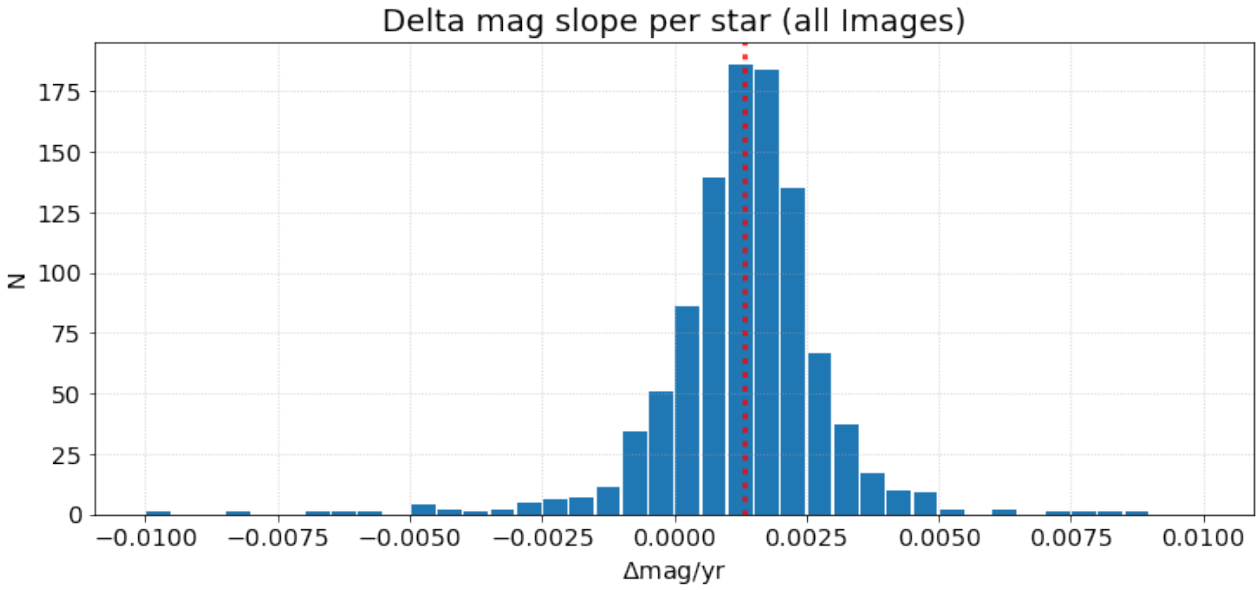

Figure 8: Slopes for the selected stars in the M4 F160W images, sampling from all of the images. The median position is denoted by the vertical red line. Note that a positive value of Δmag/yr reflects increasing magnitude (loss of measured flux).

ω Cen

Images of the outer regions of ω Cen were taken in 2016, 2018, and 2022 in both F110W and F160W (in programs 14118, 14662 and 16864, respectively). The 2016 and 2018 observations each consisted of seven three-exposure visits, while the 2022 data only contained a single three-exposure visit for F110W. The same observation strategy was used in F160W. Within each visit, the first exposure was a short exposure of 142s, followed by 1302s exposure, a large dither, and another 1302s exposure (the longer exposures in the 2018/2022 visits were both reduced to 1202s due to the shortened orbit lengths). In both filters, the first images (purple/blue points in Figures 9 and 14) appear to be brighter than the following longer exposures. However, this effect seems to be correlated to the countrates of the stars measured, as the fainter stars show the opposite behavior, possibly indicating an effect of countrate nonlinearity, which is beyond the scope of this report. As stars are only compared to themselves (and not substantially brighter/fainter sources across time), the relative measurements can still be used to analyze the sensitivity change. Variation of the brightness limits for inclusion in this analysis did not strongly impact the slope.

F110W

Stars that appeared in 30 of the 45 images or more, with STMag 23 or less, and with both magnitude standard deviations and mean PSF fit quality of 0.05 or less were selected for the analysis. The F110W median magnitude offset of all the images yielded a sensitivity change of -0.15±.04%/yr, and a sensitivity change of -0.12±.05%/yr for just the first images. The median slope for all of the images -0.15±.01%/yr, and -0.13±.01%/yr when fitting slopes to just the first images of each visit.

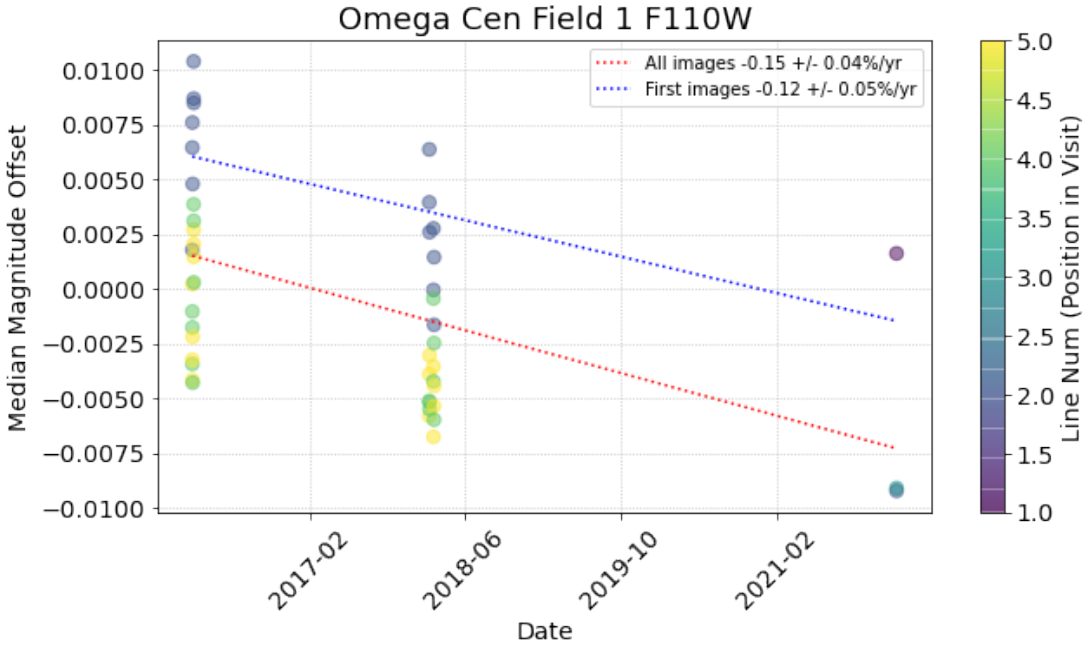

Figure 9: Median magnitude offset for the ω Cen field F110W images. The color of the points corresponds to the chronological position (LINENUM) in each visit when an exposure was taken.

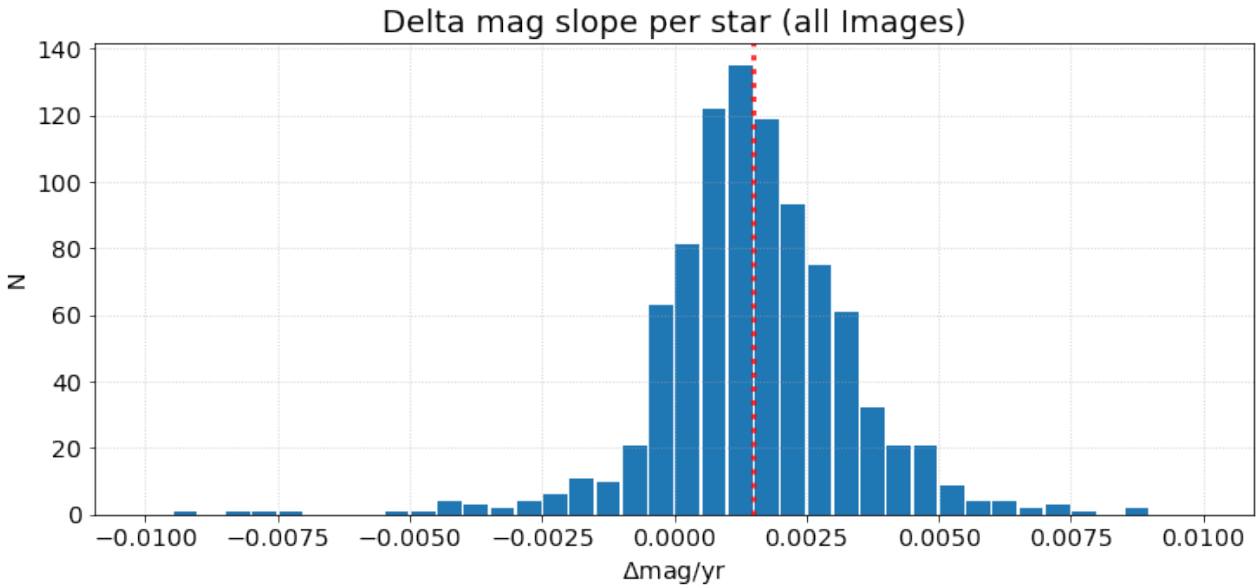

Figure 10: Slopes for the selected stars in the ω Cen F110W images, sampling from all of the images. The median position is denoted by the vertical red line. Note that a positive value of Δmag/yr reflects increasing magnitude (loss of measured flux).

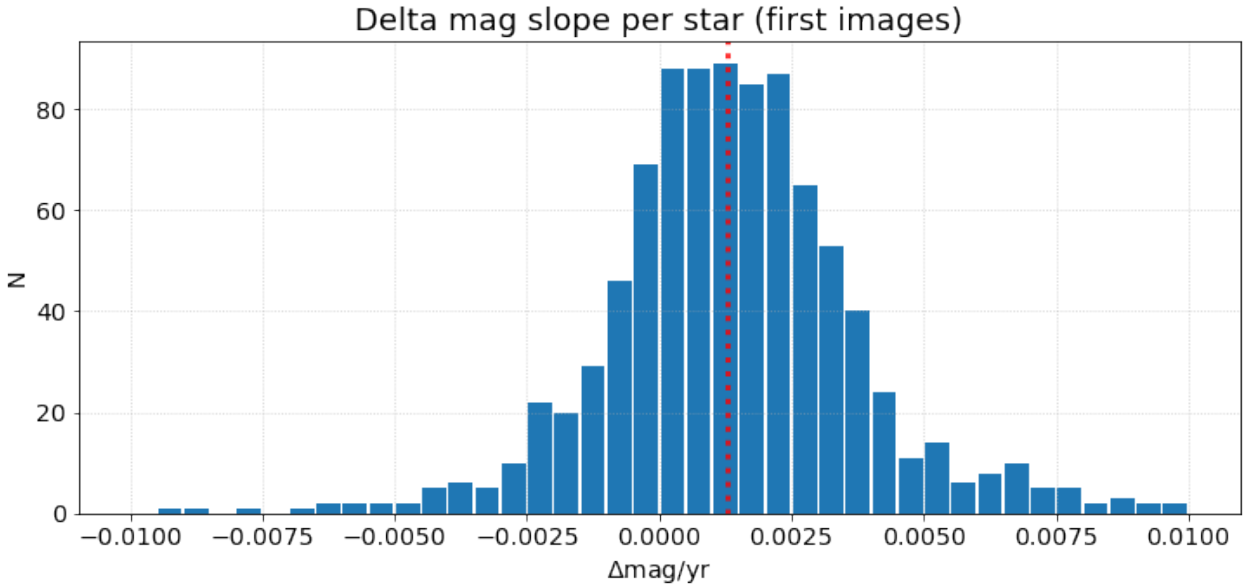

Figure 11: Slopes for the selected stars in the ω Cen F110W images, sampling from all of the images. The median position is denoted by the vertical red line. Note that a positive value of Δmag/yr reflects increasing magnitude (loss of measured flux).

F160W

The star selection criteria for the F110W were also applied for the F160W images. The F160W median magnitude offset yielded sensitivity changes of -0.13±.04%/yr and -0.16±.06%/yr for all the images and just the first images, respectively. Median slopes of -0.14±.01%/yr and -0.17±.07%/yr were calculated for the two sets of images. The uncertainty of the median slope for the first images is notably higher in this case, due to higher uncertainties in the individual slope measurements from fitting fewer images.

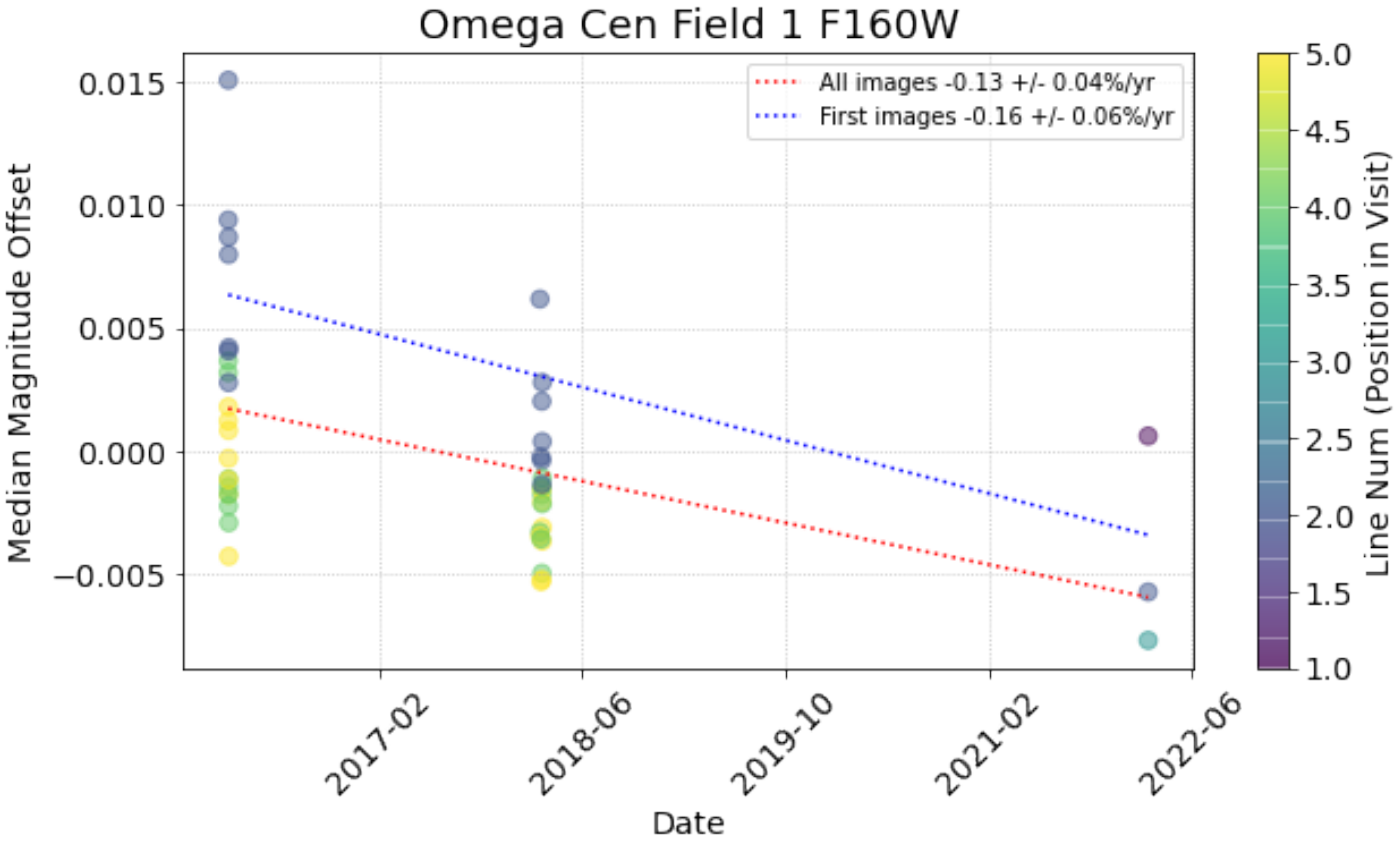

Figure 12: Median magnitude offset for the ω Cen field F160W images. The color of the points corresponds to the chronological position (LINENUM) in each visit when an exposure was taken.

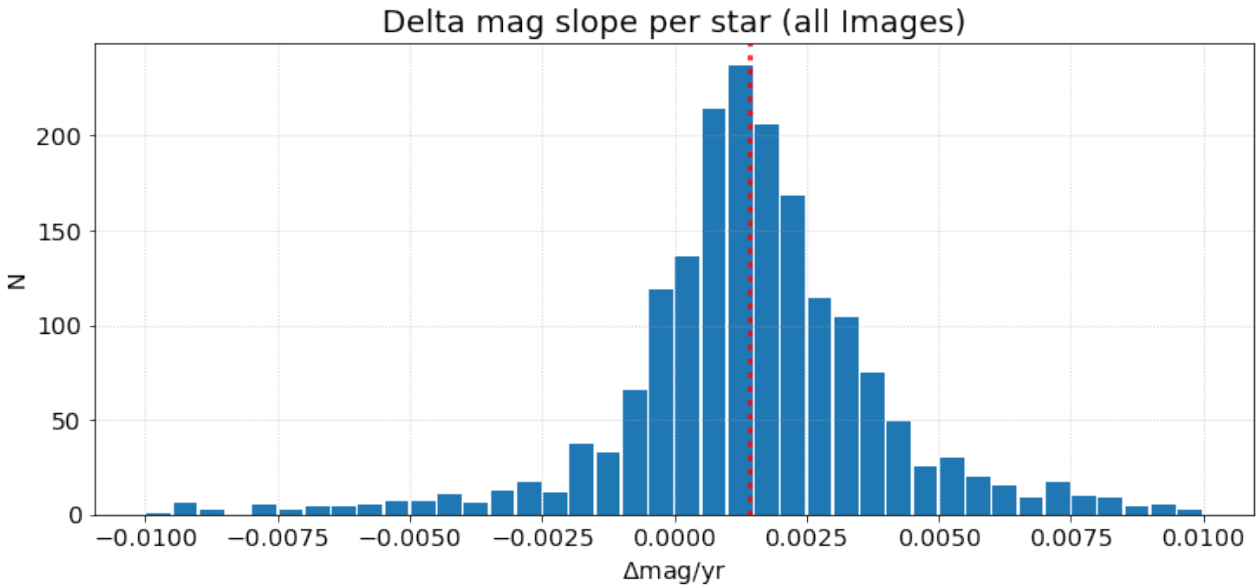

Figure 13: Slopes for the selected stars in the F160W images, sampling from all of the images. The median position is denoted by the vertical red line. Note that a positive value of Δmag/yr reflects increasing magnitude (loss of measured flux).

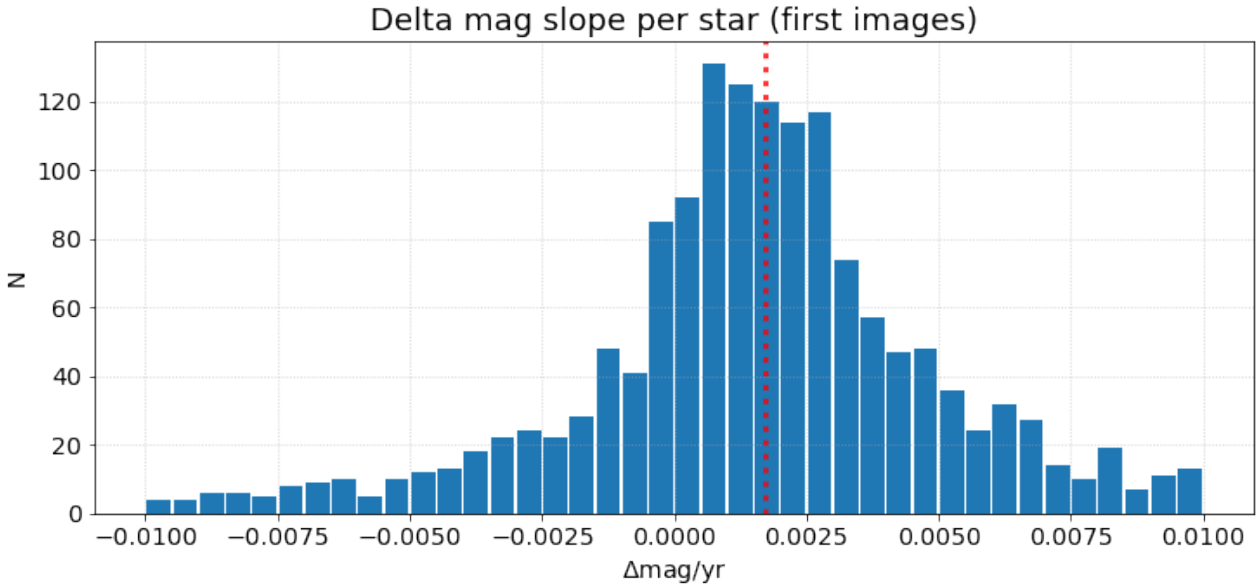

Figure 14: Slopes for the selected stars in the F160W images, sampling from the first images. The median position is denoted by the vertical red line. Note that a positive value of Δmag/yr reflects increasing magnitude (loss of measured flux).

4. ω Centauri Core

As a part of the monitoring of the astrometric calibration of WFC3/IR, the core of ω Cen has been observed consistently in F160W from 2009 to 2022. While in principle these datasets could be used to measure the sensitivity change of the IR channel, the photometric precision achievable in the core of the cluster will be substantially limited by the crowding (>10 stars/arcsec^2, when proper selection criteria are applied to the stars.

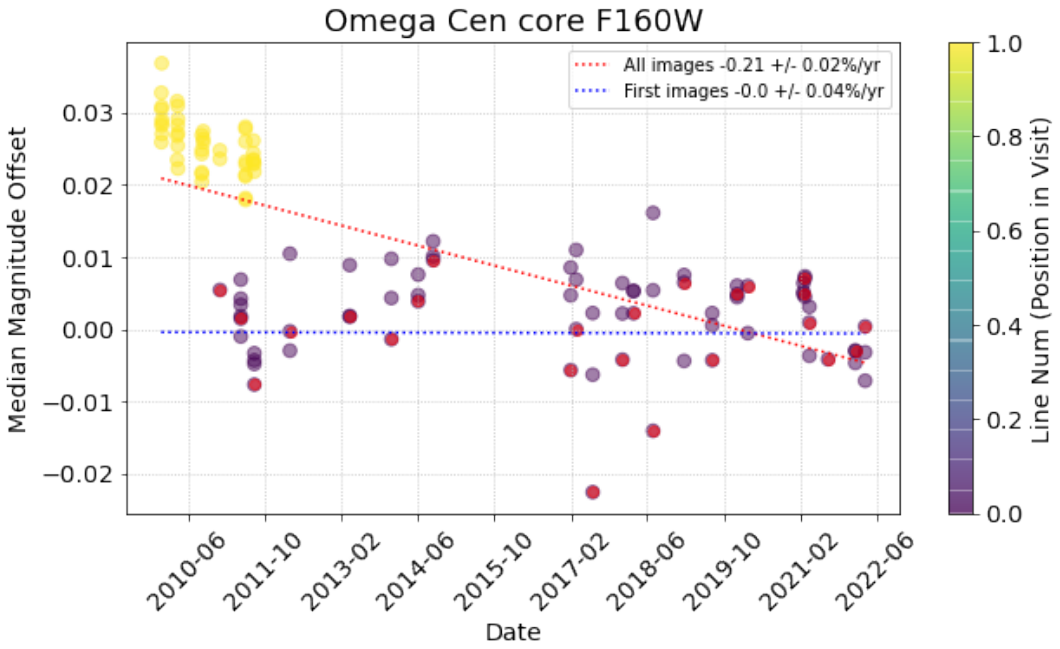

Figure 15: Median magnitude offset for the ω Cen core F160W images. The color of the points corresponds to the chronological position (LINENUM) in each visit when an exposure was taken. However, the astrometric monitoring program (in purple) uses an unconventional observation structure, which places 3 visits into a single orbit. Exposures taken at the beginning of the orbit are marked in red.

Fitting a slope to the median magnitude offset of all the images of the core of ω Cen yields a slope of -0.21 $\pm$ 0.02%/yr. However, as shown in Figure 15, the slope is substantially biased by measurements from 2009-2011. These observations were taken as part of program 11928, for geometric distortion and flatfield calibration of many WFC3/IR filters. The F160W exposures were taken after exposures in several other wide band filters, with no dithering before the F160W images. As discussed in Bajaj (2019), the resulting self persistence biases photometry to appear brighter. While the latter observations (in purple/red) were not dithered between exposures in the same orbit, the observatory was rolled by several degrees, which mimics dithering to some degree by moving stars to new pixels. However, due to the crowding of the field it is unlikely that either dithering or rolling would provide substantial persistence mitigation. In general, the crowding of the field likely significantly limits the precision of the photometry (due to contamination of nearby sources), making sensitivity losses obfuscated by other sources of error. In addition, many of the stars in the field are

saturated, and are nearby the non saturated high SNR stars, further lowering the accuracy of flux estimation via aperture photometry.

Our result for the first images of this target significantly differs from Kozhurina-Platais and S. Baggett (2020), though this is likely due to two differences in analysis. The first difference is the selection of stars used to measure the change in sensitivity. In Kozhurina-Platais and S. Baggett (2020), stars within the instrumental magnitude range [-12.5, -10] were used (ST Mag 15.5-18). However, as shown in Figure 16, stars at instrumental magnitude of -10 are already within 10% of saturation in the brightest pixel within the first read (when using the SPARS 25 sample sequence, which is used by all of the exposures of this field in this analysis). Thus, majority stars brighter than -10 would typically have no reads in which the flux in the brightest pixel would be well measured, leading to large uncertainties in the flux. In this analysis, only stars brighter than -8, and with peak pixel countrates less than 2500 were used, to ensure the stars were bright, but would have at least one unsaturated read.

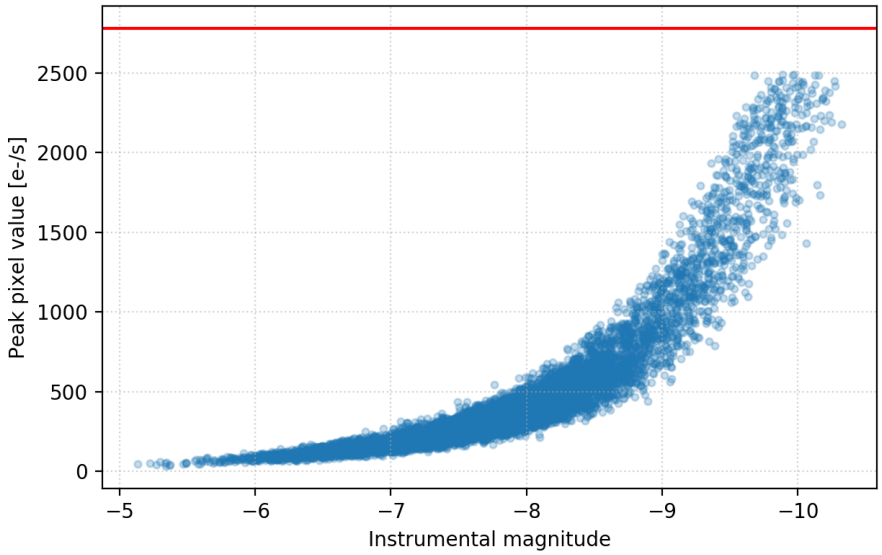

Figure 16: Peak pixel value vs instrumental magnitude for one of the exposures of the ω Cen core field. The red line denotes the countrate that achieves full well depth (saturation) in the time before the first nondestructive read. The photometry was run to specifically avoid measuring stars with peak pixel values greater than 2500. Though many stars in the images were brighter than this, they are not recorded in the catalog and thus not featured in this plot.

The second difference comes from the classification of "first images". In Kozhurina-Platais and S. Baggett (2020) images from HST programs 11928 and 12340 (shown in yellow in 15) were included in the analysis of the first images. However, while those images may have been the first exposures in F160W taken in those orbits, they were not the very first images taken in the orbit. Both programs 11928 and 12340 were flat field verification programs, and thus took exposures in several filters before F160W, and did not dither before the F160W

exposures, leading to strong persistence effects. It is our hypothesis that the persistence in these images, and the early epoch in which these images were taken strongly bias the slope more negatively, by making stars appear brighter (via persistence) rather than higher sensitivity.

5. Standard Star Comparison

The HST photometric calibration typically uses bright, isolated, nonvariable stars (standard stars) with accompanying modeled spectral energy distributions (SEDs) to compute the inverse sensitivities. However, examining the relative flux (e.g. countrates) of the standard stars flux measurements over time could, in theory, provide some insight into the senstivity loss of the detector. If a time dependent component contributed to the variation of the standard star measurements, then detrending the flux measurements should reduce the scatter (standard deviation) as shown in Calamida et al. (2021). For this experiment, we use the target/filter combinations with the most observations: GD-153/F160W. Each flux measurement was detrended using the following equation:

$$F_d = F_i \times (1 - s/100.) * (t_i - t_0)/365.25 \quad (1)$$

Where F_d is the detrended flux, F_i is the flux as measured in the image, s is the slope is the sensitivity loss per year (in percent), t_i is the exposure start time of the the image (in MJD), and t_0 is a reference epoch (in MJD), i.e. the exposure start time of the first image. The detrended fluxes were then normalized by the median of all the flux measurements, and then the standard deviation (clipped at three sigma) was calculated from the normalized measurements.

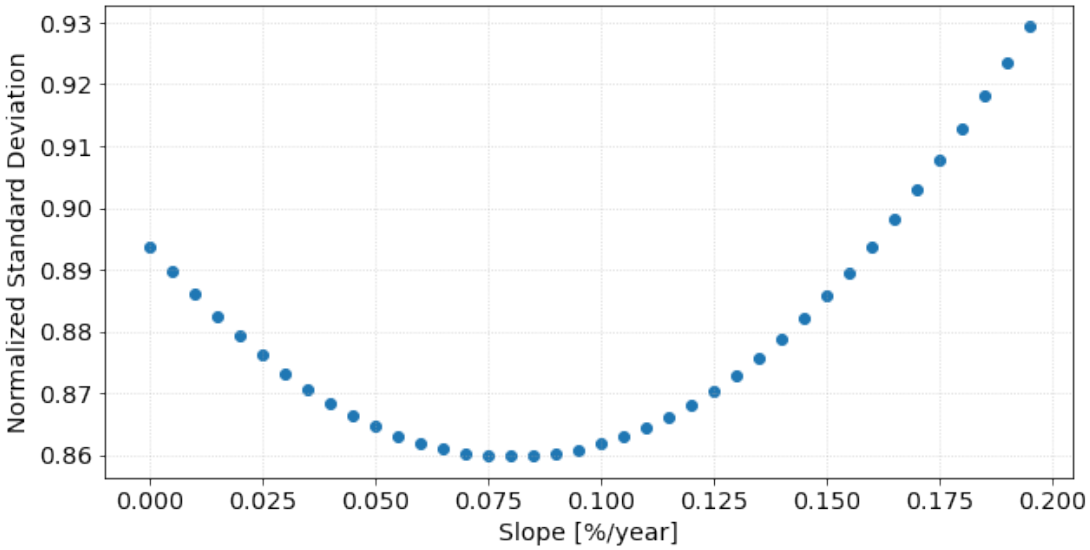

Figure 17: Standard deviation of GD-153 F160W flux values detrended across a range of sensitivity loss slopes. Note: the y-axis is in percent.

As shown in Figure 17, detrending the flux measurements for GD-153 in the F160W filters does improve the scatter of measurements. However, the overall change to the scatter is nearly negligible, dropping by approximately 0.03%, to 0.86%, compared to values that are not detrended. The resulting ineffectiveness of detrending can be seen by comparing figures 18 and 19, which show the relative flux measurements before and after detrending with a slope of 0.08%/year, corresponding to the minimum in figure 17. This is largely due to the poor repeatability of the WFC3/IR detector, which limits the precision of photometry even for images taken within the same visit, as discussed in Bajaj (2019). The heterogeneity of observation strategy (sample sequences, exposure times, dithering etc used in the monitoring over many years) as well as effect of prior observations also contribute to the visit-to-visit scatter for the standard stars, as shown in Bajaj, Calamida, and Mack (2021).

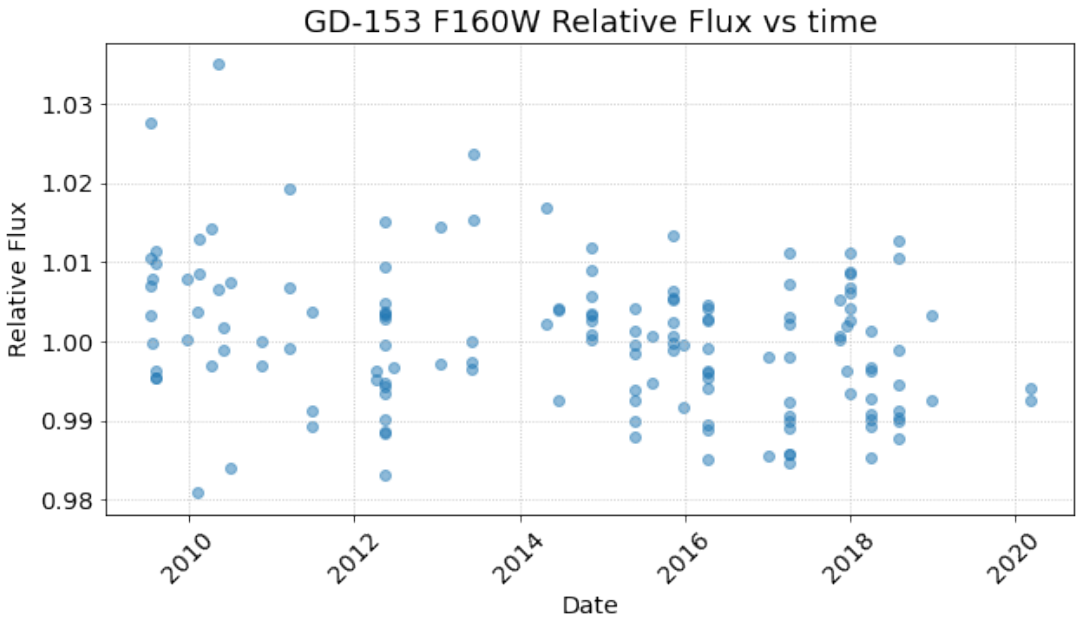

Figure 18: The normalized flux values for GD-153 F160W measurements before detrending.

As these errors are at least somewhat systematic (as opposed to random), the slopes that minimize the standard deviation can vary considerably from star to star and filter to filter. Thus, no consistent detection of the sensitivity loss change can be made from the IR standard star images. However, these observations are still important for accurately (rather than precisely) computing the zero points, due to the availability of physical models for the standard star SEDs.

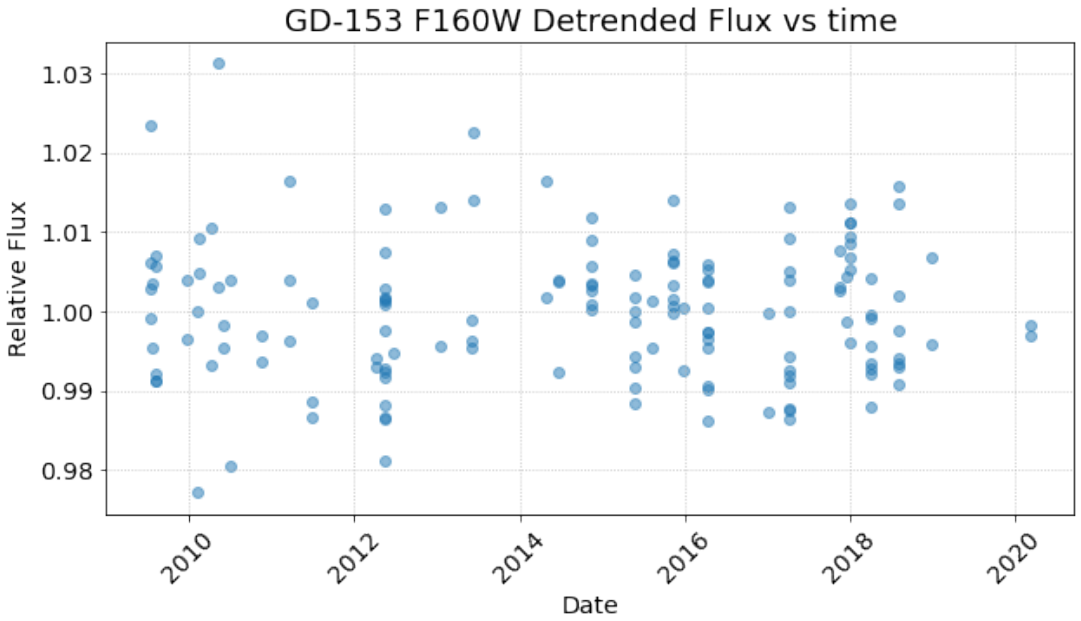

Figure 19: The normalized flux values for GD-153 F160W measurements after detrending, using the standard deviation minimizing value of 0.08%/yr.

6. Conclusions

The WFC3/IR photometric performance shows sensitivity losses when comparing consistently obtained photometric measurements over time. With the exception of the core of ω Cen, the clusters show a decrease in sensitivity of 0.1-0.2%/yr. The measurements for each field are show in Table 2.

Target	Filter	Median Slope	Median Slope (first images)
47 Tuc	F160W	-0.12%/yr	-0.10%/yr
M-4	F110W	-0.19%/yr	-0.14%/yr
M-4	F160W	-0.14%/yr	N/A
ω Cen	F110W	-0.15%/yr	-0.13%/yr
ω Cen	F160W	-0.13%/yr	-0.16%/yr
ω Cen core	F160W	-0.20%/yr	0.0%/yr
Average*	Both	-0.15%/yr	-0.13%/yr

Table 2: Summary of median slope values for the sampled stars for each of the targets. *Note: The average does not include the ω Cen core values.

In general, the sensitivity losses as measured in the first images of each of the visits observing the targets shows a slightly flatter slope (-0.13%/yr), compared to slopes extracted using all the images, -0.15%/yr. This is likely due to the early observations being more strongly affected by persistence, as persistence mitigation techniques were not employed until later on. This pushes the measured flux in many (non-first) images higher. The resulting

slopes extracted when using all the images appear artificially steeper (the first images would be substantially less affected by persistence). Thus, the true sensitivity loss is likely closer to to the .13%/yr slope from the first images.

The limiting factor in the precision measurement of the sensitivity loss is likely persistence. In theory, persistence can be modeled and potentially subtracted from images to make photometry more consistent, which could lead to better constraints on the sensitivity loss. However, the differing behavior at different time scales (Gennaro, Bajaj, and Long (2018)), intrinsic variability of persistence (Long and S. Baggett (2018)), "burping" of persistence from up to days prior (the release of persistence signal described in Ryan and S. M. Baggett (2015)), and the complex processing done in the calibration pipeline make the development and use of a general correction difficult, especially with large persistence signals at shorter timescales.

Another source of error is likely the detector calibration itself. As the data are taken at various positions and telescope orientations the stars land on varied parts of the detectors. Thus, any error in the flatfield calibration may also contribute to uncertainties in the sensitivity loss measurements, though flatfield errors are measured to be less than 0.5% - small compared to the sensitivity loss over 13 years (approximately 1.5%), though the errors are larger within 128 pixels of the edge of the detector (Dahlen (2013)).

A further consideration of the errors could be the effects focus variation on the PSF. As the telescope drifts slightly in and out of focus during the orbital cycle, due to heating/cooling, the PSF expands/contracts, changing the relative flux inside an aperture. Using larger apertures may help offset this effect, at the expense of more contamination from neighboring sources as well as incorporating lower signal-to-noise ratio pixels. However, changing aperture sizes and comparing the full width at half max of fit radial profiles did not show strong correlations with the flux differences. Variation in focus may account for some of the scatter within a visit as well.

In addition to the sources of error from the observatory itself, these measurements of cluster stars may also be partially limited by astrophysical effects. In contrast to the white dwarf standard stars, many of the stars in the clusters could be variable stars, making the relative flux measurements between epochs degenerate with changes in sensitivity. However, the effects of stellar variability would only affect the clusters with the fewest observational epochs (due to sampling effects). In the densest clusters, the proper motion of stars over a the long 13 year baseline may also lead to varying degrees of contamination for a given star over time, though this effect is likely small.

While the filters used in this analysis are the two most frequently used aboard WFC3/IR, the results of this study may not necessarily apply across the full wavelength range covered by the IR channel, and other IR filters may sustain different sensitivity change rates. If available, clusters repeatedly imaged in other filters could be used to measure sensitivity changes in those filters, though the number of cluster observations in those filters is significantly smaller. Bohlin and Deustua (2019) showed wavelength dependence in sensitivity measurements using the IR grisms, with G102 showing steeper losses than G141. Separating the flux measurements from the grism data into spectral bins could further constrain the sensitivity change over the wavelength range.

A subset of these clusters will continue to be observed in the coming years, to consistently monitor the sensitivity losses. Additional nonroutine monitoring will also be continued in

parallel using a range of observation techniques including spatial scanning (in programs 14020, 16031, 14039 described in Som and Bohlin (in prep)) as well as routine grism and staring mode observations of the standard stars.

Currently, the mechanism causing the sensitivity loss seen in WFC3/IR and other detectors aboard HST is not known. Since similar slow declines are seen in WFC3/UVIS, ACS/WFC, ACS/SBC, and STIS/CCD, it is possible the losses are due to components in the optical path preceding the detectors (i.e. the mirrors), though no definitive conclusions can be drawn at this point.

Acknowledgements

We thank M. Marinelli and A. Pidgeon of the WFC3 Photometry Calibration group and S. Baggett for their suggestions regarding analysis contained in and clarity of this report. We also thank Dr. J. Green and Professor A. Riess for their review of this document.

References

Anderson, J. (July 2022). *One-Pass HST Photometry with hst1pass*. WFC3 ISR 2022-05.

Bajaj, V. (Nov. 2017). *Aligning HST Images to Gaia: a Faster Mosaicking Workflow*. WFC3 ISR 2017-19.

— (June 2019). *WFC3/IR Photometric Repeatability*. WFC3 ISR 2019-07.

Bajaj, V., A. Calamida, and J. Mack (Apr. 2021). *Updated WFC3/IR Photometric Calibration*. WFC3 ISR 2020-10.

Bohlin, Ralph C. and Susana E. Deustua (Mar. 2019). "CALSPEC: WFC3 IR Grism Spectrophotometry". In: *arXiv e-prints*, arXiv:1903.11985, arXiv:1903.11985. arXiv: 1903.11985 [astro-ph.IM].

Bradley, Larry et al. (Oct. 2017). *astropy/photutils: v0.4*. DOI: 10.5281/zenodo.1039309. URL: https://doi.org/10.5281/zenodo.1039309.

Calamida, A. et al. (Feb. 2021). *Updated WFC3/IR Photometric Calibration*. WFC3 ISR 2021-04.

Dahlen, T. (Jan. 2013). *WFC3/IR Spatial Sensitivity Test*. WFC3 ISR 2013-01.

Davis, Lindsey (1987). *Specifications for the Aperture Photometry Package*. Tech. rep. National Optical Astronomy Observatories.

Fruchter, A. S. et al. (2010). "BetaDrizzle: A Redesign of the MultiDrizzle Package". In: *STSCI Calibration Workshop Proceedings*. Ed. by Susana Deustua and Cristina Oliveira, pp. 376–381.

Gaia Collaboration et al. (May 2021). "Gaia Early Data Release 3. Summary of the contents and survey properties". In: 649, A1, A1. DOI: 10.1051/0004-6361/202039657. arXiv: 2012.01533 [astro-ph.GA].

Gennaro, M., V. Bajaj, and K. Long (May 2018). *A characterization of persistence at short times in the WFC3/IR detector*. WFC3 ISR 2018-05.

Kozhurina-Platais, V. and S. Baggett (Apr. 2020). *WFC3 IR sensitivity over Time*. WFC3 ISR 2020-05.

Long, K. and S. Baggett (Mar. 2018). *Persistence in the WFC3 IR Detector: Intrinsic Variability*. WFC3 ISR 2018-03.

Ryan, R. E. and S. M. Baggett (July 2015). *The Internal Flat Fields for WFC3/IR*. WFC3 ISR 2015-11.

The Astropy Collaboration et al. (Jan. 2018). "The Astropy Project: Building an inclusive, open-science project and status of the v2.0 core package". In: *ArXiv e-prints*. arXiv: 1801.02634 [astro-ph.IM].

Appendices

A Target Information

In this section we present further information about the visits used in the analysis of the various targets. This information contains mainly observation details, such as the dates and dithering information.

ω Cen

The observations of ω Cen were mostly taken as a part of GO programs 14118 and 14662, with the exception of visit `ies104`, which was intentionally taken for this photometric analysis. The images were taken in groups of 3, with a short exposure, a long exposure, a large dither, and additional long exposure taken in each visit.

Visit	Proposal ID	Date-Obs	Start Time	N Images
ictj31	14118	2016-01-30	14:40:07	3
ictj32	14118	2016-01-30	19:13:59	3
ictj33	14118	2016-01-30	23:50:18	3
ictj34	14118	2016-01-31	17:22:23	3
ictj35	14118	2016-02-03	18:37:58	3
ictj36	14118	2016-02-04	00:59:53	3
ictj37	14118	2016-02-04	05:46:18	3
id8031	14662	2018-02-09	16:40:27	3
id8032	14662	2018-02-09	19:51:04	3
id8033	14662	2018-02-10	13:19:36	3
id8034	14662	2018-02-22	14:51:29	3
id8035	14662	2018-02-22	16:47:43	3
id8036	14662	2018-02-24	12:57:49	3
id8037	14662	2018-02-24	14:54:51	3
ies103	16864	2022-02-09	23:25:25	3

Table 3: Details of the F110W exposures of ω Cen outer field.

47 Tuc

The 47 Tuc observations were taken mostly as a part of the IR Linearity monitor, with the exception of visit `ies105` which was intentionally taken for this photometric analysis. The typical visit alternated long and short exposures, often followed by darks (not included in this analysis), with a variety of dither patterns/frequencies.

Visit	Proposal ID	Date-Obs	Start Time	N Images
ictj38	14118	2016-02-04	13:50:58	3
ictj39	14118	2016-02-04	17:13:08	3
ictj40	14118	2016-02-05	02:27:16	3
ictj41	14118	2016-02-05	04:02:43	3
ictj42	14118	2016-02-05	05:38:10	3
ictj43	14118	2016-02-05	07:13:36	3
ictj44	14118	2016-02-05	18:21:40	3
id8038	14662	2018-02-24	17:20:25	3
id8039	14662	2018-02-24	19:19:50	3
id8040	14662	2018-02-25	17:35:53	3
id8041	14662	2018-02-25	19:32:36	3
id8042	14662	2018-02-20	05:38:33	3
id8043	14662	2018-02-25	00:05:52	3
id8044	14662	2018-02-22	21:13:03	3
ies104	16864	2022-02-16	09:24:58	3

Table 4: Details of the F160W exposures of ω Cen outer field.

Visit	Proposal ID	Date-Obs	Start Time	N Images
ibbw04	11931	2010-03-13	17:30:54	16
ibbw08	11931	2010-07-13	13:12:12	16
ibbw09	11931	2010-11-20	09:16:27	16
ibmg20	12352	2011-04-09	19:41:24	3
ibmg21	12352	2011-04-18	12:39:17	3
ibmg22	12352	2011-04-13	16:08:13	4
ibmg23	12352	2011-09-16	00:42:05	3
ibmg24	12352	2011-09-18	21:04:18	3
ibmg25	12352	2011-09-11	07:49:20	4
ibvl10	12696	2012-02-14	02:10:56	3
ibvl11	12696	2012-02-18	01:58:56	3
ibvl12	12696	2012-02-26	18:53:33	4
ibvl22	12696	2012-08-05	21:33:53	3
ibvl23	12696	2012-08-22	20:24:40	3
ibvl24	12696	2012-08-10	00:27:14	4
ic5n1e	13079	2013-04-19	07:28:41	3
ic5n2e	13079	2013-04-18	02:27:53	3
icfh01	13563	2013-12-21	05:11:53	3
icfh02	13563	2013-12-23	01:00:49	3
ies105	16864	2022-02-08	01:17:13	4

Table 5: Details of the F160W exposures of 47 Tuc.

Messier 4

The F110W observations in visit `ibqj01` of M4 were taken in a two-orbit visit using the filter as part of HST GO Program 12602. Each of these orbits consisted of four medium length

exposures with the `WFC3-IR-DITHER-BOX-MIN` pattern used after each exposure with a line distance of 4.5 pixels, returning to the same position at the beginning of following orbit. The remaining observations used the same exposure times, but were dithered by approximately 40 pixels between successive exposures. The F160W observations in visit `ibqj02` of M4 were taken using the same strategy as `ibqj01`, but were used for four concurrent orbits (rather than two). The remaining F160W observations were taken after he F110W exposures in the corresponding visits, with the same large dithers.

Visit	Proposal ID	Date-Obs	Start Time	N Images
ibqj01	12602	2012-04-16	19:43:56	8
id7j01	14725	2017-03-27	01:13:20	4
id7j02	14725	2017-07-25	20:13:18	4
iejw01	16512	2021-08-30	21:56:12	2
iejw02	16512	2022-02-28	18:33:58	2

Table 6: Details of the F110W exposures of M4.

Visit	Proposal ID	Date-Obs	Start Time	N Images
ibqj02	12602	2012-04-20	20:46:09	16
iejw01	16512	2021-08-30	23:31:38	2
iejw02	16512	2022-02-28	18:57:58	2

Table 7: Details of the F160W exposures of M4.

ω Cen core

The majority of the ω Cen core observations were taken as part of the WFC3/IR astrometric monitoring/calibration programs. The exposures were all approximately 250 seconds long in the F160W filter. Note that the 1-image visits are actually subvisits of a single orbit (each orbit is made of 3 subvisits for these observations). All of the exposures in the 1-image visits were rolled by approximately 10 degrees. The exposures in the programs 11928 and 12340 were all proceeded by observation in other filters, and used very little dithering.

Visit	Proposal ID	Date-Obs	Start Time	N Images
ibcj01	11928	2009-12-10	18:38:26	3
ibcj02	11928	2009-12-12	21:40:52	3
ibcj03	11928	2009-12-13	18:32:40	3
ibcj04	11928	2010-03-21	08:57:04	3
ibcj05	11928	2010-03-24	15:14:03	3
ibcj06	11928	2010-03-26	08:41:37	3
ibcj07	11928	2010-09-03	03:12:55	3
ibcj08	11928	2010-08-25	01:59:11	3
ibcj09	11928	2010-08-25	06:46:41	3
iblq01	12340	2011-05-30	10:45:30	3
iblq02	12340	2011-05-31	13:55:57	3
iblq03	12340	2011-05-30	17:23:28	3
iblq04	12340	2011-07-19	15:26:36	2
iblqa4	12340	2011-07-19	18:23:31	3
ibm502	12353	2010-12-18	22:47:11	3
ibm509	12353	2011-04-30	18:03:13	1
ibm510	12353	2011-04-30	18:22:49	1
ibm511	12353	2011-04-30	18:41:23	1
ibm512	12353	2011-04-30	19:39:02	1
ibm513	12353	2011-04-30	19:57:53	1
ibm514	12353	2011-04-30	20:16:27	1
ibm515	12353	2011-07-25	14:33:04	3
ibm520	12353	2011-07-25	18:23:59	1
ibm521	12353	2011-07-25	18:43:35	1
ibm522	12353	2011-07-25	19:08:41	1
ibvj05	12714	2012-03-08	19:46:46	1
ibvj06	12714	2012-03-08	20:04:11	1
ibvj07	12714	2012-03-08	20:30:00	1
ic4j07	13100	2013-03-24	13:50:04	1
ic4j08	13100	2013-03-24	14:55:12	1
ic4j09	13100	2013-03-24	15:20:36	1
ich804	13570	2013-12-14	17:32:18	1
ich805	13570	2013-12-14	17:50:23	1
ich806	13570	2013-12-14	18:09:45	1
ich810	13570	2014-06-03	11:00:27	1
ich811	13570	2014-06-03	11:26:47	1
ich812	13570	2014-06-03	10:41:09	1
ich816	13570	2014-09-06	21:21:22	1
ich817	13570	2014-09-06	21:39:26	1
ich818	13570	2014-09-06	21:58:44	1
idcm04	14550	2017-01-30	09:21:27	1
idcm05	14550	2017-01-30	09:40:03	1
idcm06	14550	2017-01-30	09:59:38	1
idcm10	14550	2017-03-06	00:51:42	1

Table 8: Details of the F160W exposures of ω Cen core.

Visit	Proposal ID	Date-Obs	Start Time	N Images
idcm11	14550	2017-03-06	01:11:04	1
idcm12	14550	2017-03-06	01:30:53	1
idcm16	14550	2017-06-19	08:15:17	1
idcm17	14550	2017-06-19	08:35:05	1
idcm18	14550	2017-06-19	08:53:41	1
ido704	15000	2017-12-25	17:37:46	1
ido705	15000	2017-12-25	17:56:34	1
ido706	15000	2017-12-25	18:15:22	1
ido710	15000	2018-03-06	01:38:24	1
ido711	15000	2018-03-06	01:56:56	1
ido712	15000	2018-03-06	02:15:32	1
ido716	15000	2018-07-08	10:15:42	1
ido717	15000	2018-07-08	10:35:07	1
ido718	15000	2018-07-08	10:53:57	1
idv704	15593	2019-01-22	07:57:33	1
idv705	15593	2019-01-22	08:23:02	1
idv706	15593	2019-01-22	08:48:02	1
idv716	15593	2019-07-20	12:03:16	1
idv717	15593	2019-07-20	12:22:04	1
idv718	15593	2019-07-20	12:40:52	1
ie8804	15733	2019-12-26	00:02:21	1
ie8805	15733	2019-12-26	00:21:45	1
ie8806	15733	2019-12-26	01:35:01	1
ie8810	15733	2020-03-03	03:28:49	1
ie8811	15733	2020-03-03	04:27:37	1
ieg904	16413	2021-02-20	06:50:26	1
ieg905	16413	2021-02-20	07:08:46	1
ieg906	16413	2021-02-20	07:27:06	1
ieg910	16413	2021-03-02	03:38:43	1
ieg911	16413	2021-03-02	03:57:03	1
ieg912	16413	2021-03-02	04:15:23	1
ieg918	16413	2021-07-27	10:07:05	1
ieg990	16413	2021-03-30	11:37:15	1
ieg991	16413	2021-03-30	11:55:35	1
ieg992	16413	2021-03-30	13:00:27	1
iem404	16588	2022-01-17	00:34:35	1
iem405	16588	2022-01-17	00:54:54	1
iem406	16588	2022-01-17	01:15:09	1
iem410	16588	2022-03-20	14:58:59	1
iem411	16588	2022-03-20	15:17:19	1
iem412	16588	2022-03-20	15:35:34	1

Table 9: Details of the F160W exposures of ω Cen core (cont'd).